

DGNS: Deformable Gaussian Splatting and Dynamic Neural Surface for Monocular Dynamic 3D Reconstruction

Xuesong Li^{1,2}, Jinguang Tong^{1,2}, Jie Hong³, Vivien Rolland², Lars Petersson²
¹Australian National University, ²CSIRO, Australia, ³The University of Hong Kong

Abstract

Dynamic scene reconstruction from monocular video is critical for real-world applications. This paper tackles the dual challenges of dynamic novel-view synthesis and 3D geometry reconstruction by introducing a hybrid framework—Deformable Gaussian Splatting and Dynamic Neural Surfaces (DGNS), in which both modules can leverage each other for both tasks. During training, depth maps generated by the deformable Gaussian splatting module guide the ray sampling for faster processing and provide depth supervision within the dynamic neural surface module to improve geometry reconstruction. Simultaneously, the dynamic neural surface directs the distribution of Gaussian primitives around the surface, enhancing rendering quality. To further refine depth supervision, we introduce a depth-filtering process on depth maps derived from Gaussian rasterization. Extensive experiments on public datasets demonstrate that DGNS achieves state-of-the-art performance in both novel-view synthesis and 3D reconstruction. <https://github.com/Benzlxs/DGNS>

1. Introduction

Most scenes in our world are dynamic in nature and achieving dynamic scene reconstruction from monocular video can empower robots with strong perception capabilities, essential to many real-world applications. Dynamic scene reconstruction primarily involves two key tasks: dynamic novel-view generation and 3D reconstruction. In the field of dynamic novel-view synthesis, several approaches [15, 26, 27, 43] have extended neural radiance fields (NeRF) [37] by incorporating feature grid planes or implicit deformation fields. Another line of work [24, 60, 61] models dynamic scenes using explicit Gaussian representations, such as 3D Gaussian Splatting (3DGS) [23]. While these approaches have achieved promising visual quality, they struggle to accurately recover the 3D geometry of dynamic scenes. For 3D geometry reconstruction in dynamic scenes, some methods [3] have combined deformation fields with implicit surface representations—specifically, SDF in canonical space.

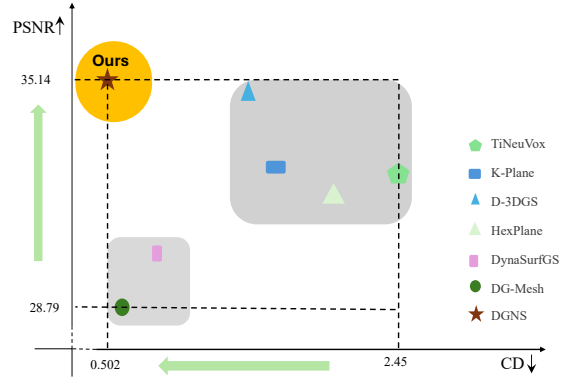


Figure 1. Comparison between different methods, the higher PSNR, the better. The smaller CD, the better. Methods that represent the best of both should be located in the top-left area.

Other approaches [4, 29] utilize deformable 3DGS to reconstruct dynamic surfaces by introducing strong regularization to ensure that Gaussian primitives adhere to the surface. However, these methods encounter difficulties in producing high-fidelity novel-view synthesis. As illustrated in Fig. 1, current methods tend to excel either in dynamic novel-view synthesis (top-right area) or in dynamic 3D reconstruction (bottom-left area), but balancing these two tasks remains an unresolved challenge in dynamic scene reconstruction.

Motivated by the observation that robust geometry guidance can enhance, rather than diminish, rendering quality in static scene modeling [52, 64], we propose a hybrid representation that combines deformable Gaussian and dynamic neural surfaces for dynamic scene reconstruction from monocular video. In this framework, the deformable Gaussian splatting (DGS) module is optimized primarily for appearance reconstruction, while the dynamic neural surfaces (DNS) module focuses on geometry reconstruction. The depth maps generated by the DGS module guide the ray sampling process and provide supervision within the DNS module, while the signed distance function (SDF) learned in the DNS module informs the distribution of Gaussian primitives around the surface. To mitigate the noise in depth supervision for the DNS module, we employ Gaussian rasterization to render two types of depth maps— α -

blended and median depth maps—and introduce a filtering process to create an accurate depth map for supervising depth in the DNS module. As reconstruction from monocular video is a highly under-constrained optimization problem, we introduce the normal supervision for both modules. We conducted extensive experiments on two public datasets, where our method outperformed existing approaches on both novel-view synthesis and 3D reconstruction tasks. Our primary contributions are as follows:

- We propose a hybrid representation of deformable Gaussian and dynamic neural surfaces, marking a pioneering advancement in monocular dynamic 3D reconstruction. Our approach surpasses state-of-the-art performance in both novel-view synthesis and geometry reconstruction.
- We introduce a simple yet effective depth-filtering process for depth maps generated through Gaussian rasterization, enhancing the accuracy of depth supervision.
- We perform extensive comparative experiments on public datasets for both novel-view synthesis and geometry reconstruction, demonstrating the advantages of our method over existing approaches.

2. Related work

View synthesis for dynamic scene: View synthesis for dynamic scenes is both challenging and crucial for 3D modeling. NeRF [37] has shown impressive capabilities in generating high-fidelity novel views for static scenes by using Multi-Layer Perceptrons (MLPs) to model the radiance field, which is then rendered into pixel colors through neural volumetric techniques. Extensions of NeRF to dynamic scenes [15, 26, 27, 31, 43, 47] use time-conditioned latent codes and explicit deformation fields to capture temporal variations. However, the reliance on NeRFs’ extensive point sampling along each ray and the computational demands of MLPs limit their scalability for dynamic scenes. To address these limitations, studies have introduced techniques such as hash encoding [38, 48], explicit voxel grids [10, 12, 14, 54], and feature grid planes [5, 7, 13, 45], which have accelerated training and improved performance in handling dynamic scenes. Another line of research explores geometric primitive rasterization using point clouds [1, 55, 62], offering computational efficiency and flexibility, though these methods often encounter challenges with discontinuities and outliers. More recently, 3DGS [23] has emerged as a promising approach, leveraging anisotropic 3D Gaussians as rendering primitives. These Gaussians are depth-ordered and projected onto a 2D plane through alpha-blending, enabling high-quality real-time rendering. Various approaches have extended 3DGS to dynamic scenes [21, 24, 33, 60, 61]. For example, [33] introduced dynamic 3DGS by iteratively optimizing the Gaussians per frame, while [21, 53, 61] used deformation fields to model temporal changes in Gaussian distributions. Despite these advancements, such techniques

remain primarily focused on novel-view synthesis and often struggle to capture scene geometry accurately, resulting in limitations in high-quality surface extraction.

Dynamic surface reconstruction: Reconstructing dynamic surfaces from monocular video is essential for applications such as intelligent robotics and virtual reality. Traditional approaches often depend on predefined object templates [6, 20, 68] or temporal tracking [11, 16, 67]. With advances in neural implicit 3D representations [37, 40], methods like LASR [56] and ViSER [57] reconstruct articulated shapes using differentiable rendering techniques [30], while BANMo [58] and PPR [59] apply NeRF to dynamic scenes, and SDFFlow [35] models dynamic motion by estimating derivatives of the SDF value. Other approaches utilize RGB-D data to incorporate depth information, improving supervision for dynamic object modeling. Examples include SobolevFusion [46], OcclusionFusion [28], NDR [3], and DynamicFusion [39]. Recently, 3DGS has been integrated into several methods to enhance optimization speed and robustness. Examples include MoSca [25], Dg-mesh [29], MoGS [34], DynaSurfGS [4], and Shape-of-Motion [50]. Specifically, Dg-mesh [29] introduces Gaussian-mesh anchoring to ensure Gaussians are evenly distributed, tracking mesh vertices over time and producing high-quality meshes using a differential Poisson solver [42]. Shape-of-Motion [50] employs data-driven priors, such as monocular depth maps and 2D tracks, to constrain Gaussian motion, while DynaSurfGS [4] combines Gaussian features from 4D neural voxels with planar-based splatting for high-quality rendering and surface reconstruction. Despite progress, a fidelity gap persists due to the explicit regularization of Gaussian primitives, which restricts rendering quality relative to D-3DGS. Our approach addresses this with surface-aware density control of Gaussian, improving 3D reconstruction while maintaining high fidelity.

3. Preliminary

3.1. Deformable 3DGS

3DGS [23] uses Gaussian primitives to represent a static scene, achieving high-quality rendering fidelity. Each Gaussian primitive is defined with a center (x_i), a covariance matrix Σ_i , an opacity σ_i , and spherical harmonics coefficients h_i , i.e. $G_i = \{x_i, \Sigma_i, \sigma_i, h_i\}$. When rendering novel-view images, the 3D Gaussian primitives are projected onto the 2D image plane and then combined using α -blending through a tile-based differentiable rasterizer. The color $C(p)$ of a pixel p is computed as follows:

$$C(p) = \sum_{i \in N} c_i \alpha_i \prod_{j=1}^{i-1} (1 - \alpha_j^{2D}), \alpha_i = \sigma_i e^{-\frac{1}{2}(p - \mathbf{x}_i)^T \Sigma_i (p - \mathbf{x}_i)} \quad (1)$$

where Σ_i is the 2D projection of the 3D Gaussian’s covariance matrix. The rasterization process accumulates each Gaussian contribution efficiently, enabling high-quality rendering. However, standard 3DGS is limited to static scenes

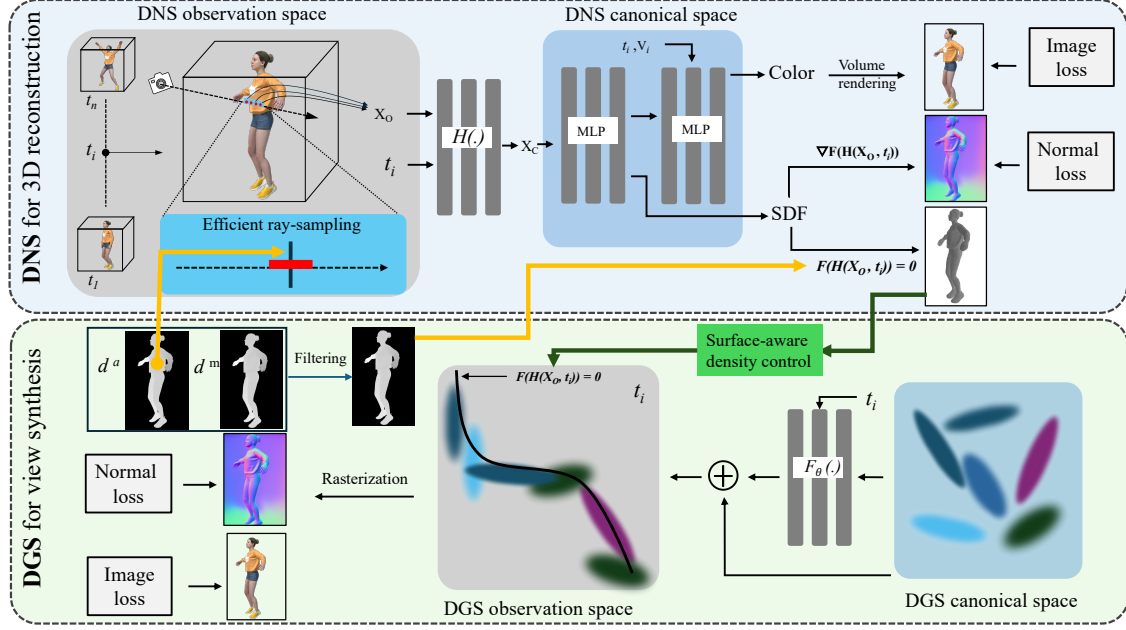


Figure 2. The framework of DGNS consists of two primary modules: the top module, DNS, for 3D reconstruction, and the bottom module, DGS, for view synthesis. There are three key interactions between these modules. The **orange arrows** represent the information flow from DGS to DNS, including efficient ray-sampling and filtered depth supervision. The **blue arrow** illustrates the information flow from DNS to DGS, implementing surface-aware density control.

and cannot model temporal changes.

To extend 3DGS to dynamic scenes, Deformable 3DGS (D-3DGS) [61] incorporates a deformation field that models time-dependent changes in position, rotation, and scale. Each Gaussian in canonical space is dynamically transformed by applying offsets calculated through a deformation MLP network F_θ , i.e. $(\delta \mathbf{x}, \delta \mathbf{r}, \delta \mathbf{s}) = F_\theta(\gamma(\mathbf{x}), \gamma(t))$, $F_\theta(\cdot)$, where $\gamma(\cdot)$ denotes positional encoding, \mathbf{x} is the Gaussian’s canonical position, and t is the current time step. The deformed Gaussian at time t is expressed as: $G(\mathbf{x} + \delta \mathbf{x}, \mathbf{r} + \delta \mathbf{r}, \mathbf{s} + \delta \mathbf{s}, \sigma)$.

The rasterization pipeline remains differentiable, allowing gradients to backpropagate through the Gaussian parameters and the deformation network during optimization. This framework handles both temporal consistency and fine-grained motion, achieving high-quality rendering.

3.2. Dynamic Neural SDF

SDF represents the object’s geometry by learning the signed distance of each point in a 3D space relative to the object’s surface. Formally, the surface S of an object is represented as the zero-level set of the SDF, defined by:

$$S = \{x \in \mathbb{R}^3 \mid \mathcal{F}(x) = 0\} \quad (2)$$

where $d(x)$ is the SDF value at a point x . Opacity used in 3DGS or NeRF can be derived from SDF value using a logistic function [49]. Neural Dynamic Reconstruction (NDR) [3] extends SDF to model dynamic objects by incorporating a deformation field. The deformation field pro-

vides a homeomorphic (continuous and bijective) mapping $\mathcal{H}(\cdot, t): \mathbb{R}^3 \rightarrow \mathbb{R}^3$, which maps x_o of deformable observation space at time t to its corresponding point x_c in a canonical 3D space, where the SDF is defined independently of time or motion. This formulation ensures that any point on the dynamic surface is described accurately by setting $d(x_c) = 0$. The Dynamic Neural Surface can be defined by

$$ds = \{x \in \mathbb{R}^3 \mid \mathcal{F}(x_c) = \mathcal{F}(\mathcal{H}(x_o, t)) = 0\} \quad (3)$$

The deformation field $\mathcal{H}(\cdot)$ is designed strictly invertible, allowing a point x_o in canonical space to map back to any observed frame t via the inverse transformation H^{-1} . Invertibility of \mathcal{H} enforces a cycle-consistent constraint across frames, which is an important regularization for modeling dynamic scenes [51].

4. Method

Current approaches for dynamic scene reconstruction typically excel in either novel-view synthesis or 3D geometry reconstruction, but not both. Our framework, illustrated in Fig. 2, introduces a hybrid representation that combines Deformable Gaussian Splatting and Dynamic Neural Surfaces modules, with both components jointly optimized to enhance performance across both tasks. The details of each module are presented in the following sections.

4.1. DNS for dynamic surface reconstruction

The DNS module utilizes the deformation field defined in Eq.3 to map the dynamic observation space to canonical

space. Unlike other dynamic SDF methods[3], our approach incorporates ray-sampling with depth proposals and depth supervision from the DGS module. Additionally, our method introduces normal supervision using surface normals from a foundation model.

Efficient ray-sampling: Ray-sampling can be computationally intensive without prior information [37], as exhaustive sampling is needed to approximate a pixel’s color from an unknown density distribution accurately. Efficiency can be improved by selectively sampling in non-empty regions of the scene. NeRF’s hierarchical volume sampling scheme uses a coarse model to approximate a density distribution, guiding the sampling of the fine model and increasing computational efficiency. In addition to hierarchical sampling, two other major sampling schemes are proposal-based [2] and occupancy-based [19, 63]. Proposal-based methods, like Mip-NeRF 360 [2], replace the coarse model with a compact proposal model that produces only density rather than both density and color. Occupancy-based methods, such as PlenOctree [63], effectively filter out points with a low density, avoiding unnecessary sampling. While these coarse-to-fine strategies [2, 37, 44, 49] improve efficiency, they often require costly rendering processes. In our framework, we use the depth map generated by the DGS branch to eliminate unnecessary queries in empty or occluded regions, thereby speeding up the ray-sampling process. The DGS depth map provides proximity to the surface, constraining the sampling range. Specifically, the α -blending depth map d^α defines these sampling boundaries, and d^α is calculated as follows:

$$d^\alpha = \sum_{i \in N} d_i \alpha_i \prod_{j=1}^{i-1} (1 - \alpha_j) / \sum_{i \in N} \alpha_i \prod_{j=1}^{i-1} (1 - \alpha_j) \quad (4)$$

where N represents the count of 3D Gaussians encountered, d_i is the distance from the i -th Gaussian to the camera, and α_i denotes opacity. The sampling process starts by emitting a ray from the camera center, \vec{o} , along a direction \vec{v} . The ray-sampling points in observation space are taken near $\vec{o} + d^\alpha \cdot \vec{v}$, with the range adjusted based on the SDF values s calculated at ray-sampling points, $d = \mathcal{F}(\mathcal{H}(\vec{o} + d^\alpha \cdot \vec{v}, t))$, where \mathcal{F} is to predict the SDF value for a point in observation space. The sampling interval along the ray (\vec{o}, \vec{v}) in observation space is from $\vec{o} + (d^\alpha - s|d|) \cdot \vec{v}$ to $\vec{o} + (d^\alpha + s|d|) \cdot \vec{v}$, in which the s is a scaling factor that adjusts based on the predicted SDF value.

Depth and normal regularization Recovering dynamic 3D structures from monocular video is a highly under-constrained optimization problem. Additional depth cues, such as RGB-D sensors or monocular depth estimation, are usually introduced to improve the reconstruction [3, 28, 39]. The efficient ray-sampling mechanism can provide a rough sampling range but does not directly optimize the SDF in canonical space. The α -blending depth tends to be noisy, especially in the edge regions, as shown in Fig. 3 (b). To

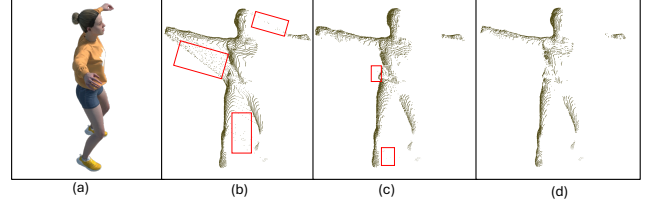


Figure 3. Visualization of the depth map in 3D space. The right-most is the RGB image, images from left to right are 3D point clouds projected from α -blending depth, median depth, and filtered depth.

avoid the depth floaters around depth boundaries, the median depth is calculated with Gaussian rasterization simultaneously. The median depth of a ray is the depth of the Gaussian center which causes the accumulated rays’ transmittance to drop below a threshold τ_d . Therefore, $d^m = d_k$ if $T_{k-1} \geq \tau_d$ and $T_k < \tau_d$, where $T_i = \prod_{j=1}^{i-1} (1 - \alpha_j)$, and τ_d is set to 0.6 in our experiment. The median depth is visualized in Fig. 3 (c), and we can observe that there are still floaters around the surface due to the transmittance drop. To generate an accurate depth map for supervising the DNS, we propose a simple but effective filtering process, in which the depth is treated as a reliable prediction as long as the median depth and α -blending one are close enough (i.e., smaller than τ_f), as follows:

$$d^f = \begin{cases} (D^\alpha - D^m)/2, & \text{if } |d^\alpha - d^m| < \tau_f \\ 0, & \text{if } |D^\alpha - D^m| \geq \tau_f \end{cases} \quad (5)$$

Filtered points are on the surface with SDF loss, as follows:

$$\mathcal{L}_{\text{sdf}} = \sum_{d^f \in \mathcal{D}} \|\mathcal{F}(\mathcal{H}(\vec{o} + d^f \cdot \vec{v}, t))\|_1 \quad (6)$$

Apart from depth cues, we add the normal supervision to relieve the under-constrained optimization problem. The monocular normal foundation models, such as Marigold [22, 36], are used to generate the pseudo normal map \bar{N} . Similar to MonoSDF [47], we use the volume rendering method to calculate the normal of ray \mathbf{r} , denoted as \hat{N} , which is a weighted sum of each ray-sampling point normal, $\nabla_{\mathbf{x}_o} \mathcal{F}(\mathcal{H}(x_o, t))$, on the ray \mathbf{r} . The consistency between the volume rendered normal map \hat{N} and the predicted monocular normal map \bar{N} is imposed with angular and $L1$ loss [47, 65], as follows

$$\mathcal{L}_{\text{dn}}^n = \frac{1}{N} \sum_{\mathbf{r} \in \mathcal{R}} \left\| \hat{N}(\mathbf{r}) - \bar{N}(\mathbf{r}) \right\|_1 + \left\| 1 - \hat{N}(\mathbf{r})^\top \bar{N}(\mathbf{r}) \right\|_1 \quad (7)$$

4.2. DGS for dynamic view synthesis

In contrast to existing methods using the 3DGS to model dynamic scenes [24, 29, 60, 61], we add the surface-aware density control, concentrating deformable 3D Gaussian points around the surface area, which enhances the model’s ability to capture both the geometry and color of

dynamic surfaces. Additionally, we incorporate surface normal supervision using normals derived from foundation models. These components are detailed below.

Surface-aware density control: Utilizing the object’s surface can serve as effective guidance for positioning Gaussian primitives to enhance rendering quality [32, 52, 64]. However, directly aligning Gaussian primitives to the surface often causes a decline in rendering quality [18, 66]. To address this, we adopt a surface-aware density control strategy, similar to GSDF [64] for static scenes, to optimize the distribution of Gaussian primitives. Specifically, the zero-level set of DNS (Eq.3) in observation space is used to guide Gaussian growth (split/clone) and pruning operations. Gradient-based adaptive density control[23] and the SDF values of Gaussian primitives from the DNS module are employed to fine-tune Gaussian placement and density. For each Gaussian primitive \mathbf{x}_g in DGS canonical space, we determine its location in observation space as $(\mathbf{x}_g + \delta\mathbf{x}_g)$, where $(\delta\mathbf{x}_g, \delta\mathbf{r}_g, \delta\mathbf{s}_g) = F_\theta(\gamma(\mathbf{x}_g), \gamma(t))$ through the GS deformation field. The SDF distance of \mathbf{x}_g is then calculated as $d_g = \mathcal{F}(\mathcal{H}(\mathbf{x}_g + \delta\mathbf{x}_g, t))$. Accordingly, the criteria for Gaussian growth are defined as follows:

$$\epsilon_g = \nabla_{\mathbf{x}_g} + w_g \phi(d_g), \quad (8)$$

where $\nabla_{\mathbf{x}_g}$ represents the average gradient of \mathbf{x}_g , w_g is a weighting parameter which controls the influence of geometric factors, and $\phi(x) = \exp(-x^2/2\sigma^2)$ is inversely proportional to the SDF value. When ϵ_g is larger than a threshold τ_g , the new Gaussians will be added. In addition to adding Gaussians, the SDF distance can be used to prune Gaussian primitives that lie far from the surface. The pruning criteria are customized as follows:

$$\epsilon_p = \sigma_p - w_p(1 - \phi(d_g)), \quad (9)$$

where σ_p is the sum of opacity across K iterations and the weighting parameter w_p controls the influence of the SDF distance on running criteria. Gaussian primitives will be removed if ϵ_p is below a set threshold τ^p .

Normal supervision: To ease the under-constrained optimization problem of monocular dynamic scene reconstruction, we add the normal loss to regularize the GS module. The normal direction of each Gaussian primitive can be approximated with the direction of the axis with the minimum scaling factor [8]. The normal in the world coordinate system is defined as: $\mathbf{n} = \mathbf{R}[k, :] \in \mathbb{R}^3$, $k = \arg \min([s_1, s_2, s_3])$, where s_1, s_2, s_3 are the Gaussian scales and \mathbf{R} is the Gaussian rotation matrix. Similar to rendering color Eq. (1), the normal vector of a point p in the screen space can be rendered as $\hat{N}^g(p) = \sum_{i \in N} n_i \alpha_i \prod_{j=1}^{i-1} (1 - \alpha_j)$. Therefore, the normal regularization loss can be calculated as:

$$\mathcal{L}_{\text{dg}}^n = \frac{1}{N} \sum_{p \in \mathcal{P}} \left\| \hat{N}^g(p) - \bar{N}(p) \right\|_1 + \left\| 1 - \hat{N}^g(p)^\top \bar{N}(p) \right\|_1 \quad (10)$$

4.3. Optimization

For the GS module, the image loss measures the difference between the rendered RGB images and ground truth images and usually includes two rendering losses \mathcal{L}_1 and $\mathcal{L}_{\text{ssim}}$, supplemented by a normal loss.

$$\mathcal{L}_{\text{dg}} = \lambda_I \mathcal{L}_1 + (1 - \lambda_I) \mathcal{L}_{\text{ssim}} + \lambda_{\text{gn}} \mathcal{L}_{\text{dg}}^n \quad (11)$$

where λ_I and λ_{gn} are the weighting coefficients. Similarly, the image loss in the DNS module is supervised by the \mathcal{L}_1 loss. The SDF will be regularized by Eikonal loss \mathcal{L}_{eik} [17]. Moreover, the SDF is supervised by the filtered point which generated the \mathcal{L}_{sdf} as Equ 6.

$$\mathcal{L}_{\text{dn}} = \mathcal{L}_1 + \lambda_{\text{sdf}} \mathcal{L}_{\text{sdf}} + \lambda_{\text{nn}} \mathcal{L}_{\text{dn}}^n + \lambda_{\text{eik}} \mathcal{L}_{\text{eik}} \quad (12)$$

where λ_{sdf} , λ_{nn} , and λ_{eik} are the weighting parameters for each loss term. The final total loss will be

$$\mathcal{L} = \mathcal{L}_{\text{dg}} + \mathcal{L}_{\text{dn}} \quad (13)$$

5. Experiments

5.1. Setup

Dataset and baseline: In the main body of this work, we conducted experimental evaluations on two public monocular video datasets (i.e. D-NeRF [43] and Dg-mesh [29]). Evaluations on other monocular video datasets, such as Nerfies [41], are included in the Supplementary material. D-NeRF includes eight sets of dynamic scenes featuring complex motion, such as articulated objects and human actions. Dg-mesh provides six sets of dynamic scenes with ground truth for each object’s deformable 3D structure. Both datasets have images at an 800×800 resolution, with 100 to 200 images per scene. To demonstrate the effectiveness of our method, we compared it with seven baselines: D-NeRF [43], NDR [3], K-Plane [13], HexPlane [5], TiNeuVox [10], Dg-mesh [29], and D3DGS [61]. D-NeRF, TiNeuVox, and NDR use implicit representations with a deformation field to map the dynamic observation space to static canonical space, while K-Plane and HexPlane employ 4D feature volumes with volume factorization. In contrast, Dg-mesh and D3DGS rely on explicit 3D Gaussian representations to model dynamic scenes. Our method integrates SDF and 3D Gaussians, achieving state-of-the-art performance in both 3D reconstruction and view synthesis.

Implementation: For the NS module, we utilize the bijective mapping network [3, 9] to learn the deformation field to mapping points from observation space back to canonical space, and canonical space is the hybrid of hash-grid encoders and 4-layer MLP for speedup. The deformation field in the GS module is learned with 8-layer MLP with 256 feature channels. GS takes around 10k iterations to make an accurate depth prediction, from which depth guidance

Method	Duck			Horse			Bird		
	CD ↓	EMD ↓	PSNR ↑	CD ↓	EMD ↓	PSNR ↑	CD ↓	EMD ↓	PSNR ↑
D-NeRF	0.934	0.073	29.79	1.685	0.280	25.47	1.532	0.163	23.85
NDR	2.235	0.083	24.79	0.359	0.148	27.23	0.444	0.130	25.43
K-Plane	1.085	0.055	33.36	1.480	0.239	28.11	0.742	0.131	23.72
HexPlane	2.161	0.090	32.11	1.750	0.199	26.78	4.158	0.178	22.19
TiNeuVox	0.969	0.059	34.33	1.918	0.246	28.16	8.264	0.215	25.55
D-3DGS	1.643	0.1146	36.76	0.941	0.203	35.66	1.398	0.138	29.38
Dg-mesh	0.790	0.047	32.89	0.299	0.168	27.10	0.557	0.128	22.98
GNS ² (ours)	0.773	0.046	37.39	0.289	0.142	35.52	0.440	0.126	30.23

Method	Beagle			Torus2sphere			Girlwalk		
	CD ↓	EMD ↓	PSNR ↑	CD ↓	EMD ↓	PSNR ↑	CD ↓	EMD ↓	PSNR ↑
D-NeRF	1.001	0.149	34.47	1.760	0.250	24.23	0.601	0.190	28.63
NDR	0.747	0.106	28.39	1.767	0.176	25.19	0.482	0.158	29.98
K-Plane	0.810	0.122	38.33	1.793	0.161	31.22	0.495	0.173	32.12
HexPlane	0.870	0.115	38.03	2.190	0.190	29.71	0.597	0.155	31.77
TiNeuVox	0.874	0.129	38.97	2.115	0.203	28.76	0.568	0.184	32.81
D-3DGS	0.898	0.211	38.56	1.487	0.193	30.22	0.883	0.270	38.75
Dg-mesh	0.639	0.117	34.53	1.607	0.172	26.61	0.726	0.136	28.64
GNS ² (ours)	0.643	0.101	39.29	0.456	0.153	29.76	0.413	0.124	38.64

Table 1. Mesh reconstruction and rendering quality results of our method compared with other baselines. Reconstructed meshes are measured with Chamfer Distance (CD) and Earth Mover Distance (EMD) with the ground truth mesh. Rendering quality is measured with Peak Signal-to-Noise Ratio (PSNR). The color of each cell indicates the **best**, **second**, and **third** score, and the third best results. In general, our method produces a better reconstruction and rendering quality among all metrics.

for ray and SDF supervision in NS starts. After the 15k iteration warm-up, the geometry guidance for density control in GS begins from 15k iterations. Joint optimization lasts for 25k iterations. All experiments were conducted on an NVIDIA RTX A6000 GPU with 48GB memory.

5.2. Results

Dg-mesh dataset: The Dg-mesh dataset [29] provides geometrical ground truth for dynamic objects at each time-frame, enabling a thorough quantitative evaluation of our method, DGNS, for both 3D reconstruction and novel-view synthesis tasks across six objects. As shown in Tab 1, our method consistently achieves the lowest CD and EMD scores across nearly all object categories. This performance highlights DGNS’s ability to capture fine-grained dynamic spatial structures with higher accuracy than competing methods, while also surpassing baselines in rendering quality. In terms of reconstruction accuracy, Dg-mesh frequently ranks second, especially in achieving lower CD and EMD scores, yet this comes with a noticeable compromise in rendering quality. Conversely, while D3DGS exhibits competitive performance in novel-view synthesis, it fails to achieve the same low CD and EMD scores necessary for high-accuracy 3D reconstruction. Our method is unique in offering consistently superior performance across both 3D reconstruction and rendering quality, providing a

comprehensive solution for tasks requiring both structural precision and visual fidelity.

The qualitative results, presented in Fig 4, further substantiate these findings, showing that meshes reconstructed by DGNS most closely resemble the ground truth. For example, Gaussian-based methods like D3DGS [61] struggle with surface accuracy due to floating Gaussian points, resulting in less cohesive 3D surfaces. While Dg-mesh [29] improves upon this with an anchoring process to reduce floating points, the resultant surface still lacks sufficient detail and smoothness. The NDR [3] method encounters challenges with specific object parts, such as accurately reconstructing the legs in *Girlwalk*, the tails of *Bird*, and the inner surface of *Torus2sphere*.

D-NeRF dataset: The comparison of our method against baselines is presented in Tab 2, demonstrating that our method, DGNS, provides a robust balance across PSNR, SSIM, and LPIPS metrics across various scenes. This balance underscores its effectiveness in novel-view synthesis tasks. While D3DG slightly outperforms our method in rendering quality across some scenes, DGNS consistently surpasses other baselines, including Dg-mesh, the method previously noted for its efficacy in 3D reconstruction.

Notably, in the D-NeRF dataset, mesh ground truths are unavailable. Thus, we have supplemented the quantitative analysis with a qualitative comparison, shown in Fig 5. The

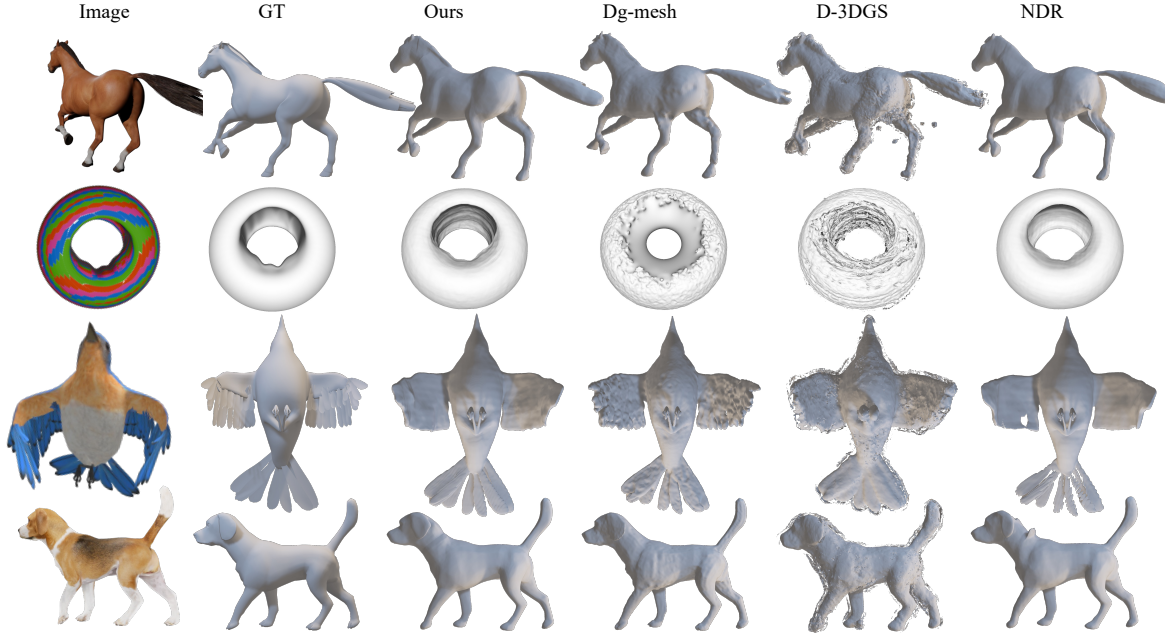


Figure 4. Qualitative comparison on the Dg-mesh dataset. The samples, from top to bottom, are *Horse*, *Torus2sphere*, *Bird*, and *Beagle*. Compared to other baselines, our results are the closest to the ground truth (GT).



Figure 5. Qualitative comparison on the D-NeRF dataset. The samples from right to left are *Hellwarrior* and *Standup*. Our method can achieve 3D reconstructions with smooth surfaces.

qualitative assessment reveals that our method yields superior performance in 3D reconstruction fidelity, even when visually assessed against high-performing baselines. Although D3DGS achieves top scores in rendering quality, it does not maintain the structural accuracy in 3D reconstruction that our method consistently delivers. In contrast, our method demonstrates state-of-the-art rendering quality while excelling in structural reconstruction, presenting a compelling solution for applications requiring both high fidelity in visual output and accurate 3D geometry. More qualitative results are included in the Supplementary material.

5.3. Ablation study

Surface-aware density control: To illustrate the effect of surface-aware density control, we present two samples of

3D reconstructions with and without surface-aware density control in Fig. 6. The results show that, in the absence of surface-aware density control, a greater number of points are dispersed away from the surface, resulting in a floating appearance. In contrast, applying surface-aware density control, points are more concentrated and closely aligned with the surface, demonstrating improved reconstruction fidelity and surface adherence.

Depth and normal supervision: The ablation study results in Tab 3 highlight the complementary effects of depth and normal information on the quality of 3D reconstruction and novel-view synthesis. When neither depth nor normal data is used, the model exhibits its lowest performance, underscoring the limitations of relying solely on other cues. Adding either depth or normal information individually leads to noticeable improvements, with depth

Method	Hell Warrior			Mutant			Hook			Bouncing Balls		
	PSNR \uparrow	SSIM \uparrow	LPIPS \downarrow	PSNR \uparrow	SSIM \uparrow	LPIPS \downarrow	PSNR \uparrow	SSIM \uparrow	LPIPS \downarrow	PSNR \uparrow	SSIM \uparrow	LPIPS \downarrow
D-NeRF	24.06	0.944	0.071	30.31	0.967	0.039	29.02	0.960	0.055	38.17	0.989	0.032
NDR	31.58	0.971	0.035	29.83	0.958	0.049	26.62	0.952	0.071	36.34	0.986	0.039
TiNeuVox	27.10	0.964	0.077	31.87	0.961	0.047	30.61	0.960	0.059	40.23	0.993	0.044
Tensor4D	31.26	0.975	0.024	29.11	0.965	0.056	24.47	0.943	0.064	26.56	0.992	0.044
K-Planes	24.58	0.952	0.084	32.50	0.951	0.066	28.12	0.949	0.052	40.05	0.993	0.032
D-3DG	41.54	0.987	0.023	42.63	0.995	0.005	37.42	0.987	0.014	41.01	0.995	0.009
Dg-mesh	25.46	0.959	0.074	30.40	0.968	0.055	27.88	0.954	0.074	29.15	0.969	0.099
GNS ² (ours)	41.68	0.988	0.023	41.47	0.984	0.011	36.34	0.979	0.023	40.71	0.994	0.012

Method	Lego			T-Rex			Stand Up			Jumping Jacks		
	PSNR \uparrow	SSIM \uparrow	LPIPS \downarrow	PSNR \uparrow	SSIM \uparrow	LPIPS \downarrow	PSNR \uparrow	SSIM \uparrow	LPIPS \downarrow	PSNR \uparrow	SSIM \uparrow	LPIPS \downarrow
D-NeRF	25.56	0.936	0.082	30.61	0.967	0.054	33.13	0.978	0.036	32.70	0.978	0.039
NDR	24.54	0.936	0.084	23.47	0.963	0.047	30.22	0.961	0.047	29.02	0.957	0.043
TiNeuVox	26.64	0.953	0.078	31.25	0.967	0.048	34.61	0.980	0.033	33.49	0.977	0.041
Tensor4D	23.24	0.942	0.089	23.86	0.954	0.054	26.30	0.938	0.056	24.20	0.925	0.067
K-Planes	28.91	0.970	0.035	30.43	0.970	0.031	33.10	0.979	0.031	31.11	0.971	0.047
D-3DG	33.07	0.979	0.018	38.10	0.993	0.010	44.62	0.995	0.006	37.72	0.990	0.013
Dg-mesh	21.29	0.838	0.159	28.95	0.959	0.065	30.21	0.974	0.051	31.77	0.980	0.045
GNS ² (ours)	29.48	0.974	0.026	37.68	0.989	0.012	44.81	0.996	0.007	38.60	0.993	0.011

Table 2. Rendering quality results of our method compared with other baselines. Our method is closely aligned with the state-of-the-art D-3DGS, yet significantly outperforms other baseline methods.



Figure 6. Demonstration of surface-aware density control. The middle image in each sample shows the mesh from the DGS module with surface-aware density control, while the rightmost image shows the result without density control.

Depth	Normals	CD \downarrow	EMD \downarrow	PSNR \uparrow
\times	\times	1.006	0.134	34.89
\times	\checkmark	0.831	0.126	35.11
\checkmark	\times	0.697	0.121	35.03
\checkmark	\checkmark	0.502	0.116	35.14

Table 3. Ablation study of depth and normal supervision.

contributing more to spatial alignment accuracy, while normals enhance surface detail and orientation. This suggests that each type of information addresses different aspects of the reconstruction task. When both depth and normal data are combined, the model achieves optimal performance across all metrics, indicating the complementary roles of these inputs. Depth data enhances spatial positioning, while normals provide detailed surface cues, resulting in a more accurate and coherent 3D reconstruction. This improved 3D structure also benefits novel-view synthesis by addressing the challenges of monocular dynamic reconstruction, a highly under-constrained optimization problem. Overall, the results emphasize that while depth and normal information each offer unique benefits, integrating both is crucial for achieving high fidelity in 3D reconstructions and producing realistic novel views.

6. Conclusion

This paper presented our method DGNS, a hybrid framework combining Deformable Gaussian Splatting and Dynamic Neural Surfaces to address the challenges of novel-view synthesis and 3D reconstruction in dynamic scenes. Through surface-aware density control, efficient ray-sampling, and depth supervision, our approach leverages interactions between DGS and DNS to achieve state-of-the-art rendering and geometric accuracy, closely aligning with ground truth and outperforming existing baselines. Experiments on D-NeRF and Dg-mesh datasets demonstrate the robustness of DGNS across complex dynamic scenes, offering a scalable solution for both geometry and appearance modeling.

Limitation: This work primarily addresses the concerns around accuracy as in Fig 1 1, although DGNS incorporates efficient ray-sampling, the DNS module still requires substantial computational resources and longer convergence times compared to DGS, making it the primary speed bottleneck in the framework. Additionally, including both modules during the training stage increases the overall memory footprint, which may limit scalability and efficiency, especially on large datasets or scenes with high complexity.

Future work: Future work will focus on enhancing the computational efficiency of MLP-based DNS modules and extending DGNS’s application to handle more complex dynamic scenes.

References

- [1] Kara-Ali Aliev, Artem Sevastopolsky, Maria Kolos, Dmitry Ulyanov, and Victor Lempitsky. Neural point-based graphics. In *Computer Vision–ECCV 2020: 16th European Con-*

- ference, Glasgow, UK, August 23–28, 2020, *Proceedings, Part XXII 16*, pages 696–712. Springer, 2020. 2
- [2] Jonathan T. Barron, Ben Mildenhall, Dor Verbin, Pratul P. Srinivasan, and Peter Hedman. Mip-NeRF 360: Unbounded Anti-Aliased Neural Radiance Fields. In *2022 IEEE/CVF Conference on Computer Vision and Pattern Recognition (CVPR)*, pages 5460–5469, 2022. 4
 - [3] Hongrui Cai, Wanquan Feng, Xuetao Feng, Yan Wang, and Juyong Zhang. Neural surface reconstruction of dynamic scenes with monocular rgb-d camera. *Advances in Neural Information Processing Systems*, 35:967–981, 2022. 1, 2, 3, 4, 5, 6
 - [4] Weiwei Cai, Weicai Ye, Peng Ye, Tong He, and Tao Chen. Dynasurfsg: Dynamic surface reconstruction with planar-based gaussian splatting. *arXiv preprint arXiv:2408.13972*, 2024. 1, 2
 - [5] Ang Cao and Justin Johnson. Hexplane: A fast representation for dynamic scenes. In *Proceedings of the IEEE/CVF Conference on Computer Vision and Pattern Recognition*, pages 130–141, 2023. 2, 5
 - [6] David Casillas-Perez, Daniel Pizarro, David Fuentes-Jimenez, Manuel Mazo, and Adrien Bartoli. The isowarp: the template-based visual geometry of isometric surfaces. *International Journal of Computer Vision*, 129(7):2194–2222, 2021. 2
 - [7] Anpei Chen, Zexiang Xu, Andreas Geiger, Jingyi Yu, and Hao Su. Tensorf: Tensorial radiance fields. In *European conference on computer vision*, pages 333–350. Springer, 2022. 2
 - [8] Hanlin Chen, Chen Li, and Gim Hee Lee. Neusg: Neural implicit surface reconstruction with 3d gaussian splatting guidance. *arXiv preprint arXiv:2312.00846*, 2023. 5
 - [9] Laurent Dinh, Jascha Sohl-Dickstein, and Samy Bengio. Density estimation using real nvp. *arXiv preprint arXiv:1605.08803*, 2016. 5
 - [10] Jiemin Fang, Taoran Yi, Xinggang Wang, Lingxi Xie, Xiaopeng Zhang, Wenyu Liu, Matthias Nießner, and Qi Tian. Fast dynamic radiance fields with time-aware neural voxels. In *SIGGRAPH Asia 2022 Conference Papers*, pages 1–9, 2022. 2, 5
 - [11] Yao Feng, Haiwen Feng, Michael J Black, and Timo Bolkart. Learning an animatable detailed 3d face model from in-the-wild images. *ACM Transactions on Graphics (ToG)*, 40(4): 1–13, 2021. 2
 - [12] Sara Fridovich-Keil, Alex Yu, Matthew Tancik, Qinlong Chen, Benjamin Recht, and Angjoo Kanazawa. Plenoxels: Radiance fields without neural networks. In *Proceedings of the IEEE/CVF conference on computer vision and pattern recognition*, pages 5501–5510, 2022. 2
 - [13] Sara Fridovich-Keil, Giacomo Meanti, Frederik Rahbæk Warburg, Benjamin Recht, and Angjoo Kanazawa. K-planes: Explicit radiance fields in space, time, and appearance. In *Proceedings of the IEEE/CVF Conference on Computer Vision and Pattern Recognition*, pages 12479–12488, 2023. 2, 5
 - [14] Wanshui Gan, Hongbin Xu, Yi Huang, Shifeng Chen, and Naoto Yokoya. V4d: Voxel for 4d novel view synthesis. *IEEE Transactions on Visualization and Computer Graphics*, 2023. 2
 - [15] Chen Gao, Ayush Saraf, Johannes Kopf, and Jia-Bin Huang. Dynamic view synthesis from dynamic monocular video. In *Proceedings of the IEEE/CVF International Conference on Computer Vision*, pages 5712–5721, 2021. 1, 2
 - [16] Philip-William Grassal, Malte Prinzler, Titus Leistner, Carsten Rother, Matthias Nießner, and Justus Thies. Neural head avatars from monocular rgb videos. In *Proceedings of the IEEE/CVF Conference on Computer Vision and Pattern Recognition*, pages 18653–18664, 2022. 2
 - [17] Amos Gropp, Lior Yariv, Niv Haim, Matan Atzmon, and Yaron Lipman. Implicit geometric regularization for learning shapes. *arXiv preprint arXiv:2002.10099*, 2020. 5
 - [18] Antoine Guédon and Vincent Lepetit. Sugar: Surface-aligned gaussian splatting for efficient 3d mesh reconstruction and high-quality mesh rendering. In *Proceedings of the IEEE/CVF Conference on Computer Vision and Pattern Recognition*, pages 5354–5363, 2024. 5
 - [19] Tao Hu, Shu Liu, Yilun Chen, Tiancheng Shen, and Jiaya Jia. EfficientNeRF: Efficient Neural Radiance Fields. *Proceedings of the IEEE/CVF Conference on Computer Vision and Pattern Recognition (CVPR)*, pages 12892–12901, 2022. 4
 - [20] Navami Kairanda, Edith Tretschk, Mohamed Elgharib, Christian Theobalt, and Vladislav Golyanik. f-sft: Shape-from-template with a physics-based deformation model. In *Proceedings of the IEEE/CVF Conference on Computer Vision and Pattern Recognition*, pages 3948–3958, 2022. 2
 - [21] Kai Katsumata, Duc Minh Vo, and Hideki Nakayama. An efficient 3d gaussian representation for monocular/multi-view dynamic scenes. *arXiv preprint arXiv:2311.12897*, 2023. 2
 - [22] Bingxin Ke, Anton Obukhov, Shengyu Huang, Nando Metzger, Rodrigo Caye Daudt, and Konrad Schindler. Repurposing diffusion-based image generators for monocular depth estimation. In *Proceedings of the IEEE/CVF Conference on Computer Vision and Pattern Recognition (CVPR)*, 2024. 4
 - [23] Bernhard Kerbl, Georgios Kopanas, Thomas Leimkühler, and George Drettakis. 3d gaussian splatting for real-time radiance field rendering. *ACM Trans. Graph.*, 42(4):139–1, 2023. 1, 2, 5
 - [24] Agelos Kratimenos, Jiahui Lei, and Kostas Daniilidis. Dynmf: Neural motion factorization for real-time dynamic view synthesis with 3d gaussian splatting. *arXiv preprint arXiv:2312.00112*, 2023. 1, 2, 4
 - [25] Jiahui Lei, Yijia Weng, Adam Harley, Leonidas Guibas, and Kostas Daniilidis. Mosca: Dynamic gaussian fusion from casual videos via 4d motion scaffolds. *arXiv preprint arXiv:2405.17421*, 2024. 2
 - [26] Tianye Li, Mira Slavcheva, Michael Zollhoefer, Simon Green, Christoph Lassner, Changil Kim, Tanner Schmidt, Steven Lovegrove, Michael Goesele, Richard Newcombe, et al. Neural 3d video synthesis from multi-view video. In *Proceedings of the IEEE/CVF Conference on Computer Vision and Pattern Recognition*, pages 5521–5531, 2022. 1, 2
 - [27] Zhengqi Li, Simon Niklaus, Noah Snavely, and Oliver Wang. Neural scene flow fields for space-time view synthesis of dynamic scenes. In *Proceedings of the IEEE/CVF Conference*

- on *Computer Vision and Pattern Recognition*, pages 6498–6508, 2021. 1, 2
- [28] Wenbin Lin, Chengwei Zheng, Jun-Hai Yong, and Feng Xu. Occlusionfusion: Occlusion-aware motion estimation for real-time dynamic 3d reconstruction. In *Proceedings of the IEEE/CVF Conference on Computer Vision and Pattern Recognition*, pages 1736–1745, 2022. 2, 4
- [29] Isabella Liu, Hao Su, and Xiaolong Wang. Dynamic gaussians mesh: Consistent mesh reconstruction from monocular videos. *arXiv preprint arXiv:2404.12379*, 2024. 1, 2, 4, 5, 6
- [30] Shichen Liu, Tianye Li, Weikai Chen, and Hao Li. Soft rasterizer: A differentiable renderer for image-based 3d reasoning. In *Proceedings of the IEEE/CVF international conference on computer vision*, pages 7708–7717, 2019. 2
- [31] Yu-Lun Liu, Chen Gao, Andreas Meuleman, Hung-Yu Tseng, Ayush Saraf, Changil Kim, Yung-Yu Chuang, Johannes Kopf, and Jia-Bin Huang. Robust dynamic radiance fields. In *Proceedings of the IEEE/CVF Conference on Computer Vision and Pattern Recognition*, pages 13–23, 2023. 2
- [32] Tao Lu, Mulin Yu, Linning Xu, Yuanbo Xiangli, Limin Wang, Dahua Lin, and Bo Dai. Scaffold-gs: Structured 3d gaussians for view-adaptive rendering. In *Proceedings of the IEEE/CVF Conference on Computer Vision and Pattern Recognition*, pages 20654–20664, 2024. 5
- [33] Jonathon Luiten, Georgios Kopanas, Bastian Leibe, and Deva Ramanan. Dynamic 3d gaussians: Tracking by persistent dynamic view synthesis. *arXiv preprint arXiv:2308.09713*, 2023. 2
- [34] Shaojie Ma, Yawei Luo, and Yi Yang. Reconstructing and simulating dynamic 3d objects with mesh-adsorbed gaussian splatting. *arXiv preprint arXiv:2406.01593*, 2024. 2
- [35] Wei Mao, Richard Hartley, Mathieu Salzmann, et al. Neural sdf flow for 3d reconstruction of dynamic scenes. In *The Twelfth International Conference on Learning Representations*, 2024. 2
- [36] Gonzalo Martin Garcia, Karim Abou Zeid, Christian Schmidt, Daan de Geus, Alexander Hermans, and Bastian Leibe. Fine-tuning image-conditional diffusion models is easier than you think. In *Proceedings of the IEEE/CVF Winter Conference on Applications of Computer Vision (WACV)*, 2025. 4
- [37] Ben Mildenhall, Pratul P Srinivasan, Matthew Tancik, Jonathan T Barron, Ravi Ramamoorthi, and Ren Ng. Nerf: Representing scenes as neural radiance fields for view synthesis. *Communications of the ACM*, 65(1):99–106, 2021. 1, 2, 4
- [38] Thomas Müller, Alex Evans, Christoph Schied, and Alexander Keller. Instant neural graphics primitives with a multi-resolution hash encoding. *ACM transactions on graphics (TOG)*, 41(4):1–15, 2022. 2
- [39] Richard A Newcombe, Dieter Fox, and Steven M Seitz. Dynamicfusion: Reconstruction and tracking of non-rigid scenes in real-time. In *Proceedings of the IEEE conference on computer vision and pattern recognition*, pages 343–352, 2015. 2, 4
- [40] Jeong Joon Park, Peter Florence, Julian Straub, Richard Newcombe, and Steven Lovegrove. DeepSDF: Learning continuous signed distance functions for shape representation. In *Proceedings of the IEEE/CVF conference on computer vision and pattern recognition*, pages 165–174, 2019. 2
- [41] Keunhong Park, Utkarsh Sinha, Jonathan T Barron, Sofien Bouaziz, Dan B Goldman, Steven M Seitz, and Ricardo Martin-Brualla. Nerfies: Deformable neural radiance fields. In *Proceedings of the IEEE/CVF International Conference on Computer Vision*, pages 5865–5874, 2021. 5
- [42] Songyou Peng, Chiyu Jiang, Yiyi Liao, Michael Niemeyer, Marc Pollefeys, and Andreas Geiger. Shape as points: A differentiable poisson solver. *Advances in Neural Information Processing Systems*, 34:13032–13044, 2021. 2
- [43] Albert Pumarola, Enric Corona, Gerard Pons-Moll, and Francesc Moreno-Noguer. D-nerf: Neural radiance fields for dynamic scenes. In *Proceedings of the IEEE/CVF Conference on Computer Vision and Pattern Recognition*, pages 10318–10327, 2021. 1, 2, 5
- [44] Radu Alexandru Rosu and Sven Behnke. Permutosdf: Fast multi-view reconstruction with implicit surfaces using permutohedral lattices. In *Proceedings of the IEEE/CVF Conference on Computer Vision and Pattern Recognition*, pages 8466–8475, 2023. 4
- [45] Ruizhi Shao, Zerong Zheng, Hanzhang Tu, Boning Liu, Hongwen Zhang, and Yebin Liu. Tensor4d: Efficient neural 4d decomposition for high-fidelity dynamic reconstruction and rendering. In *Proceedings of the IEEE/CVF Conference on Computer Vision and Pattern Recognition*, pages 16632–16642, 2023. 2
- [46] Miroslava Slavcheva, Maximilian Baust, and Slobodan Ilic. Sobolevfusion: 3d reconstruction of scenes undergoing free non-rigid motion. In *Proceedings of the IEEE conference on computer vision and pattern recognition*, pages 2646–2655, 2018. 2
- [47] Fengrui Tian, Shaoyi Du, and Yueqi Duan. Mononerf: Learning a generalizable dynamic radiance field from monocular videos. In *Proceedings of the IEEE/CVF International Conference on Computer Vision*, pages 17903–17913, 2023. 2, 4
- [48] Feng Wang, Zilong Chen, Guokang Wang, Yafei Song, and Huaping Liu. Masked space-time hash encoding for efficient dynamic scene reconstruction. *Advances in Neural Information Processing Systems*, 36, 2024. 2
- [49] Peng Wang, Lingjie Liu, Yuan Liu, Christian Theobalt, Taku Komura, and Wenping Wang. Neus: Learning neural implicit surfaces by volume rendering for multi-view reconstruction. *arXiv preprint arXiv:2106.10689*, 2021. 3, 4
- [50] Qianqian Wang, Vickie Ye, Hang Gao, Jake Austin, Zhengqi Li, and Angjoo Kanazawa. Shape of motion: 4d reconstruction from a single video. *arXiv preprint arXiv:2407.13764*, 2024. 2
- [51] Xiaolong Wang, Allan Jabri, and Alexei A Efros. Learning correspondence from the cycle-consistency of time. In *Proceedings of the IEEE/CVF conference on computer vision and pattern recognition*, pages 2566–2576, 2019. 3
- [52] Zian Wang, Tianchang Shen, Merlin Nimier-David, Nicholas Sharp, Jun Gao, Alexander Keller, Sanja Fidler, Thomas Müller, and Zan Gojcic. Adaptive shells for efficient neural radiance field rendering. *arXiv preprint arXiv:2311.10091*, 2023. 1, 5

- [53] Guanjun Wu, Taoran Yi, Jiemin Fang, Lingxi Xie, Xiaopeng Zhang, Wei Wei, Wenyu Liu, Qi Tian, and Xinggang Wang. 4d gaussian splatting for real-time dynamic scene rendering. In *Proceedings of the IEEE/CVF Conference on Computer Vision and Pattern Recognition*, pages 20310–20320, 2024. [2](#)
- [54] Linning Xu, Yuanbo Xiangli, Sida Peng, Xingang Pan, Nanxuan Zhao, Christian Theobalt, Bo Dai, and Dahua Lin. Grid-guided neural radiance fields for large urban scenes. In *Proceedings of the IEEE/CVF Conference on Computer Vision and Pattern Recognition*, pages 8296–8306, 2023. [2](#)
- [55] Qiangeng Xu, Zexiang Xu, Julien Philip, Sai Bi, Zhixin Shu, Kalyan Sunkavalli, and Ulrich Neumann. Pointnerf: Point-based neural radiance fields. In *Proceedings of the IEEE/CVF conference on computer vision and pattern recognition*, pages 5438–5448, 2022. [2](#)
- [56] Gengshan Yang, Deqing Sun, Varun Jampani, Daniel Vlasic, Forrester Cole, Huiwen Chang, Deva Ramanan, William T Freeman, and Ce Liu. Lasr: Learning articulated shape reconstruction from a monocular video. In *Proceedings of the IEEE/CVF Conference on Computer Vision and Pattern Recognition*, pages 15980–15989, 2021. [2](#)
- [57] Gengshan Yang, Deqing Sun, Varun Jampani, Daniel Vlasic, Forrester Cole, Ce Liu, and Deva Ramanan. Viser: Video-specific surface embeddings for articulated 3d shape reconstruction. *Advances in Neural Information Processing Systems*, 34:19326–19338, 2021. [2](#)
- [58] Gengshan Yang, Minh Vo, Natalia Neverova, Deva Ramanan, Andrea Vedaldi, and Hanbyul Joo. Banmo: Building animatable 3d neural models from many casual videos. In *Proceedings of the IEEE/CVF Conference on Computer Vision and Pattern Recognition*, pages 2863–2873, 2022. [2](#)
- [59] Gengshan Yang, Shuo Yang, John Z Zhang, Zachary Manchester, and Deva Ramanan. Ppr: Physically plausible reconstruction from monocular videos. In *Proceedings of the IEEE/CVF International Conference on Computer Vision*, pages 3914–3924, 2023. [2](#)
- [60] Zeyu Yang, Hongye Yang, Zijie Pan, Xiatian Zhu, and Li Zhang. Real-time photorealistic dynamic scene representation and rendering with 4d gaussian splatting. *arXiv preprint arXiv:2310.10642*, 2023. [1](#), [2](#), [4](#)
- [61] Ziyi Yang, Xinyu Gao, Wen Zhou, Shaohui Jiao, Yuqing Zhang, and Xiaogang Jin. Deformable 3d gaussians for high-fidelity monocular dynamic scene reconstruction. In *Proceedings of the IEEE/CVF Conference on Computer Vision and Pattern Recognition*, pages 20331–20341, 2024. [1](#), [2](#), [3](#), [4](#), [5](#), [6](#)
- [62] Wang Yifan, Felice Serena, Shihao Wu, Cengiz Öztireli, and Olga Sorkine-Hornung. Differentiable surface splatting for point-based geometry processing. *ACM Transactions on Graphics (TOG)*, 38(6):1–14, 2019. [2](#)
- [63] Alex Yu, Ruilong Li, Matthew Tancik, Hao Li, Ren Ng, and Angjoo Kanazawa. PlenOctrees for Real-time Rendering of Neural Radiance Fields. In *Proceedings of the IEEE International Conference on Computer Vision (ICCV)*, pages 5732–5741, 2021. [4](#)
- [64] Mulin Yu, Tao Lu, Linning Xu, Lihan Jiang, Yuanbo Xiangli, and Bo Dai. Gsdf: 3dgs meets sdf for improved rendering and reconstruction. *arXiv preprint arXiv:2403.16964*, 2024. [1](#), [5](#)
- [65] Chushan Zhang, Jinguang Tong, Tao Jun Lin, Chuong Nguyen, and Hongdong Li. Pmvc: Promoting multi-view consistency for 3d scene reconstruction. In *Proceedings of the IEEE/CVF Winter Conference on Applications of Computer Vision*, pages 3678–3688, 2024. [4](#)
- [66] Wenyuan Zhang, Yu-Shen Liu, and Zhizhong Han. Neural signed distance function inference through splatting 3d gaussians pulled on zero-level set. *arXiv preprint arXiv:2410.14189*, 2024. [5](#)
- [67] Michael Zollhöfer, Justus Thies, Pablo Garrido, Derek Bradley, Thabo Beeler, Patrick Pérez, Marc Stamminger, Matthias Nießner, and Christian Theobalt. State of the art on monocular 3d face reconstruction, tracking, and applications. In *Computer graphics forum*, pages 523–550. Wiley Online Library, 2018. [2](#)
- [68] Silvia Zuffi, Angjoo Kanazawa, David W Jacobs, and Michael J Black. 3d menagerie: Modeling the 3d shape and pose of animals. In *Proceedings of the IEEE conference on computer vision and pattern recognition*, pages 6365–6373, 2017. [2](#)